

# Visualization of the Intensity Field of a Focused Ultrasound Source *In Situ*

Trong N. Nguyen<sup>1</sup>, Member, IEEE, Minh N. Do, Fellow, IEEE, and Michael L. Oelze, Senior Member, IEEE

**Abstract**—In an increasing number of applications of focused ultrasound (FUS) therapy, such as opening of the blood–brain barrier or collapsing microbubbles in a tumor, elevation of tissue temperature is not involved. In these cases, real-time visualization of the field distribution of the FUS source would allow localization of the FUS beam within the targeted tissue and allow repositioning of the FUS beam during tissue motion. In this paper, in order to visualize the FUS beam *in situ*, a 6-MHz single-element transducer ( $f/2$ ) was used as the FUS source and aligned perpendicular to a linear array which passively received scattered ultrasound from the sample. An image of the reconstructed intensity field pattern of the FUS source using bistatic beamforming was then superimposed on a registered B-mode image of the sample acquired using the same linear array. The superimposed image is used to provide anatomical context of the FUS beam in the sample being treated. The intensity field pattern reconstructed from a homogeneous scattering phantom was compared with the field characteristics of the FUS source characterized by the wire technique. The beamwidth estimates at the FUS focus using the *in situ* reconstruction technique and the wire technique were 1.5 and 1.2 mm, respectively. The depth-of-field estimates for the *in situ* reconstruction technique and the wire technique were 11.8 and 16.8 mm, respectively. The FUS beams were also visualized in a two-layer phantom and a chicken breast. The novel reconstruction technique was able to accurately visualize the field of an FUS source in the context of the interrogated medium.

**Index Terms**—Beam visualization, focused ultrasound, monitoring, bistatic.

## I. INTRODUCTION

FOCUSED ultrasound (FUS) has been approved in the USA for non-invasive treatment of uterine fibroids, bone metastases, prostate cancer and essential tremor [1]–[4]. In addition, FUS has been explored for treating a number of other conditions including Alzheimer’s disease, brain tumors [5], breast cancer [6], stroke [7], multiple sclerosis [8] and many more [9], [10]. Therefore, the potential for FUS to improve clinical outcomes is high and the future will see many more applications of FUS realized clinically.

Manuscript received May 6, 2018; revised July 11, 2018; accepted July 12, 2018. Date of publication July 19, 2018; date of current version December 28, 2018. This work was supported by NIH under Grant R21NS098174. (Corresponding author: Trong N. Nguyen.)

The authors are with the Department of Electrical and Computer Engineering, Beckman Institute for Advanced Science and Technology, University of Illinois at Urbana–Champaign, Urbana, IL 61820 USA (e-mail: tnnguyen2@illinois.edu).

Color versions of one or more of the figures in this paper are available online at <http://ieeexplore.ieee.org>.

Digital Object Identifier 10.1109/TMI.2018.2857481

The main advantage to using FUS is that ultrasonic waves can be targeted to deep tissue locations noninvasively. Specific tissues can be targeted for treatment while surrounding healthy tissues can be spared by the therapy. In one approach, the energy of the FUS is absorbed in the focal region by the tissue and the resulting heating is used to preferentially kill tissues in the focal region. The temperature elevation of the tissue depends on several factors including the absorption coefficient of the tissue, the intensity of the FUS beam and perfusion [11]–[14]. If each of these factors can be quantified *in situ* beforehand, correct estimates of temperature elevations can be mapped enabling control of the therapy placement over time.

However, in practice quantifying the *in situ* intensity, the spatially and temporally-dependent absorption of the tissue, and the perfusion is difficult and fraught with inaccuracies. The inability to accurately quantify these parameters makes predicting the temperature elevations in a tissue during FUS difficult. Furthermore, tissue motion also changes the location of the beam in the patient causing changes in the dwell time at a particular location and changes in the variables used to predict temperature heating at a specific location. To overcome this, MRI has been used to guide focused ultrasound applications (MRgFUS) [15]. MRI is capable of producing maps of temperature elevations with updates every second and reported accuracies of 0.3°C [16]. However, MRI is not a perfect solution. MRI is still sensitive to tissue motion and the expense of using MRI with a compatible FUS system are very high.

In a growing number of FUS-based approaches, the goal of FUS is not to heat tissues but to cause some biological effect based on the mechanical action associated with FUS. In one application, tumors are sensitized to radiation by first treating them with microbubbles activated or collapsed via targeted FUS [17]. Another example of this approach is the use of FUS to transiently open the blood brain barrier (BBB) [18]–[20]. In these applications, temperature mapping is not required, but placement of the FUS beam in the proper location is paramount to successfully treating the targeted location. A current approach in FUS-based BBB opening is to use FUS to provide a small increase in tissue temperature in order to locate the beam in the context of the surrounding tissue using MRgFUS [21]. However, tissue motion between beam localization and actual FUS therapy application can cause mis-targeting of therapy and updates of the FUS beam location may not be provided during therapy. Therefore, the development of

a technique that could visualize the FUS beam *in situ* and place it in the context of the surrounding tissue environment is vital for FUS-based therapeutic applications involving mechanical-based bioeffects.

In this study, a technique for rapidly visualizing the beam from a FUS source *in situ* is developed and demonstrated in tissue-mimicking phantoms and biological samples. The underlying principle is that an imaging array co-aligned with a FUS source can be used to reconstruct the FUS field *in situ*. While visualization of the FUS field *in situ* does not provide a mapping of the temperature, the visualization does provide important information for monitoring FUS therapy. Controlling the placement of the FUS beam in a tissue during exposure is vital for the successful application of FUS therapy. For example, thermal lensing effects can shift the focus of the FUS source in the tissue during exposure [22]. Tissue motion can also shift the location of the FUS focus relative to the treatment region. Therefore, it is important to continuously visualize the FUS focal region in order to adjust the location of the FUS beam during therapy if the beam moves away from the targeted tissue region. Therefore, it is highly medically significant to develop techniques that can visualize the FUS beam in real time and place it in the context of tissue anatomy.

To our knowledge, minimal work has been conducted to visualize the actual FUS beam *in situ*. Lizzi *et al.* [23] utilized A-mode imaging to examine changes in the FUS intensity down a single scan line during therapy. In a very preliminary study, Fujiwara *et al.* [24] attempted to reconstruct the FUS beam in an agar phantom using an active imaging array technique. In the work of Casper *et al.* [25], a dual mode FUS/imaging array was designed to provide real time B-mode imaging and therapy with the same array transducer. While the array could provide some guidance for the FUS beam in the tissue regions including refocusing of the FUS beam to avoid obstacles like ribs, the spatial resolution of the array was low and no results have been forthcoming to demonstrate the ability of the dual mode array to visualize the FUS beam *in situ*.

Along a similar line of inquiry, passive acoustic mapping (PAM) techniques have been applied to detect and map sources of non-linear acoustic emissions, including cavitating bubbles and scattering following non-linear propagation of the incident field, during FUS therapy in the time domain [26]–[28] and in the frequency domain [29], [30]. These mapping techniques rely on source coherence and cross-correlation between array channels, and do not require synchronization between the FUS source and the receiving array. Although they do not require the precise registration between the FUS source and the imaging array, they are only able to localize the cavitation events in space. With the added synchronization, the beam mapping presented here can be localized both in space and time. An example of a comparison between the two techniques was recently shown by Burgess *et al.* [31] where synchronized passive cavitation was used to improve the axial resolution of the cavitation map. However, the exact registration between the FUS source and the imaging array was not explicitly shown in [31]. Furthermore, PAM typically utilizes a receiving array operating in a higher frequency band than then FUS transducer,

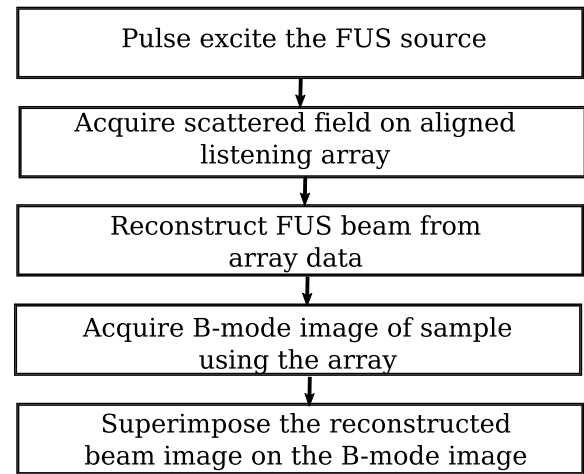


Fig. 1. Block diagram showing the steps used to reconstruct the FUS beam and visualize it in the context of surrounding structure.

to maximize the SNR of detected non-linear acoustic emissions over linear scattering. By contrast, the technique utilized here specifically seeks to map linear scattering of the incident ultrasound field as detected by the array elements operating passively.

In this study, we provide preliminary evidence that the FUS beam can be visualized using an ultrasonic array and this beam image can be superimposed on a B-mode image of an underlying sample to provide anatomical context. Specifically, the FUS source is pulse excited and the scattered field is picked up by the listening array which is synchronized through a common trigger. The FUS beam is then reconstructed by receive focusing the listening array. Next the array is used to capture a B-mode image of the sample. The reconstructed beam is then overlaid on top of the B-mode to visualize the FUS beam in the sample. Furthermore, intensity variations from the registered B-mode image can be used to adjust the reconstructed FUS beam visualization by accounting for heterogeneities in the reconstruction caused by heterogeneities in the scattered field. To quantify the accuracy of the reconstructions, the FUS beam was also reconstructed when using a thin wire target as a single scatterer that was moved throughout the field of the beam. The beam characteristics (beamwidth and depth of field) estimated from image reconstructions from the wire target were compared to the beam characteristics reconstructed from the samples.

## II. METHODS

### A. Experimental Configuration

The sequence used to visualize the FUS beam *in situ* is described by the block diagram in Fig. 1 and the excitation sequence shown in Fig. 2. Specifically, the visualization step could be conducted during FUS therapy in the off portion of the duty cycle, assuming that the FUS source is not operated at 100% duty cycle. During this short period, the FUS source can be pulse excited. The FUS source is focused only at a particular location in the sample. Therefore, assuming only single scattering events, the scattering of the FUS field will

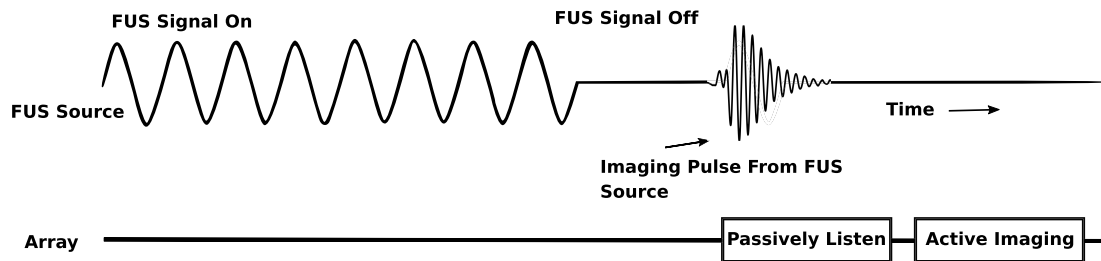


Fig. 2. Depiction of the excitation sequence for both the FUS source and the imaging array transducer.

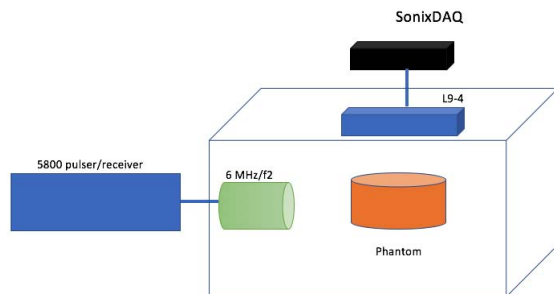


Fig. 3. Experimental setup.

only occur within the beam of the FUS source, which is targeted to a specific sample location. The intensity of the scattering of the FUS will depend on the location of the scatterer in the FUS beam and the strength of the scatterer. The scattered field is then received by the array which is triggered to begin listening once the FUS source is pulse excited. The scattered signals captured by the array are then processed to focus the array at all points in the field. After acquisition, the array used for listening is then used to capture a B-mode snapshot of the sample, providing a larger field of view of the object space. The image of the FUS source is then superimposed on top of the B-mode image of the sample providing anatomical context for targeting the FUS beam. This image can be updated for continuous monitoring of the FUS source during therapy.

To visualize the beam from a FUS source, a linear imaging array, i.e., an L9-4, was aligned with a single-element FUS transducer. The array had a measured center frequency of 5 MHz. The array consisted of 128 elements with a total length of 38 mm and element size of  $0.2698 \times 6$  mm. The  $f/2$  single-element FUS source had a center frequency of 6 MHz and a focal distance of 3.81 cm. The bandwidth of the FUS transducer and the linear array were chosen to be overlapped. In fact, the passively received RF of the linear array when imaging a tungsten wire in the bistatic setup had a center frequency of 5.3 MHz. Fig. 3 depicts the experimental setup: the FUS source, the array and the samples were submerged in degassed water.

The L9-4 linear array was operated by a SonixOne system (Ultrasonix Medical Corp., Richmond, BC, Canada) with a SonixDAQ. The SonixDAQ allowed for the pre-beamformed radio frequency (RF) data to be acquired at each element

of the array. A holder was made to align the single-element FUS transducer beam and the imaging plane of the receiving array. The holder, which houses the FUS transducer and the receiving array at a  $90^\circ$  angle, was attached to a micro-precision positioning system (Daedal Inc. Harrison City, PA). The holder was designed so that the FUS source could be translated perpendicularly to the imaging plane of the array. To ensure the imaging plane of the linear array intersected the beam of the focused source, a silicon ball with diameter smaller than 1 mm was placed on a tungsten wire ( $25 \mu\text{m}$  in diameter). The FUS source was then pulse excited using a Panametrics 5800 pulser/receiver (Olympus NDT, Waltham, MA) to transmit a pulse and receive the scattered field from the silicon ball. The FUS source was then manually displaced in the holder until the echo of the silicon sphere was visible in both the scan line recorded by the FUS source in pulse-echo mode and a B-mode image created by the array.

After the FUS source and linear array were aligned, the FUS source was operated using the sequence in Fig. 1 to visualize the FUS beam in a sample. When the array was in passive listening mode (i.e. the excitation of the array was turned off), the FUS transducer was pulse excited by the Panametrics 5800. Once the FUS transducer was pulse excited, the ultrasound waves transmitted from the FUS transducer were scattered from the sample, which was in the field of view of both the linear array and the FUS source. The imaging array was triggered in sync with the pulsed excitation and received the scattered ultrasound from the sample. The received scattered signals were then beamformed by focusing at each point in the field of the array (see below). Then, a B-mode image was constructed using the software provided by the SonixOne system. The reconstructed FUS beam was then superimposed on top of the B-mode image to visualize the beam location in the sample.

For this study, three samples were chosen to demonstrate the visualization of the beam from an FUS source *in situ*. The first sample was a homogeneous tissue-mimicking phantom made of agar embedded with glass beads having random spatial locations to provide speckle. The glass beads had diameters ranging from  $75$  to  $90 \mu\text{m}$ . The glass bead phantom provided a demonstration of the technique under ideal conditions, i.e., under homogeneous scattering conditions. The second sample was a two-layered phantom with a glass bead density contrast of 10 times between layers resulting in a 10 dB increase in intensity in the denser layer. The lower glass bead

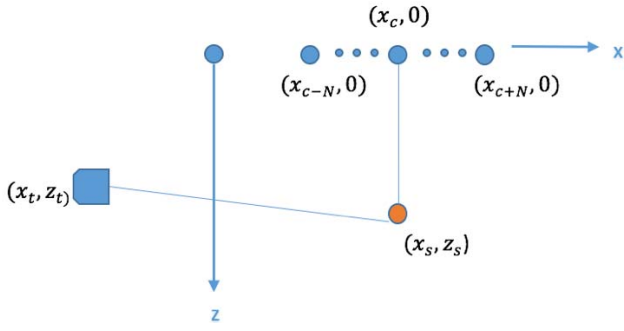


**Fig. 4.** Axes depicting the location of the FUS source at  $(x_t, z_t)$  with respect to the listening array. The FUS transducer is on the left and the array is at the top of the diagram. The point target is located at  $(x_s, z_s)$ . These axes were used to calculate the location of the FUS beam for registration with a B-mode image produced from an array scan. The subaperture of size  $2N+1$  is depicted on the x-axis from elements  $x_{c-N}$  to  $x_{c+N}$ .

density layer had the same density as the first sample, i.e., the homogeneous phantom. This second sample was chosen to demonstrate the ability of the technique to visualize the beam from a FUS source across regions that would provide different intensities. The final sample was a chicken breast, which was chosen to demonstrate the ability of the technique to visualize the beam in tissue samples where scattering is not guaranteed to be homogeneous.

## B. Passive Reconstruction Methods

**1) Registration of FUS Transducer and Linear Array:** Ideally, the array used for visualizing the FUS beam would be aligned along the axis of the FUS source. Such a configuration would occur if the FUS source had a center cutout and an array could be placed facing in the same direction as the FUS source. It should be noted that our technique will work for both the monostatic and bistatic configurations. However, due to the unavailability of a FUS transducer with a center cutout, a bistatic configuration was utilized to demonstrate the beam visualization (see Fig. 4). As a result, registration of the FUS beam with the imaging plane of the listening array was not trivial. To correctly register the beam of the FUS source in the B-mode image of the linear array, the position of the FUS source with respect to the linear array had to be estimated. The diagram in Fig. 4 shows the focused source at  $(x_t, z_t)$  and a point target at  $(x_s, z_s)$ . The linear array lies on the x axis and the first element of the array coincides with the origin  $(0, 0)$ . The z axis is the imaging depth. The goal is to estimate  $(x_t, z_t)$  with respect to the origin, which defines the location of the listening array. The time delay from the focused source  $(x_t, z_t)$  to the point target  $(x_s, z_s)$  is:

$$\tau_1(x_s, z_s) = \frac{1}{c} \sqrt{(x_s - x_t)^2 + (z_s - z_t)^2}. \quad (1)$$

Here we assume the speed of sound  $c$  to be 1540 m/s. The time delay from the point target  $(x_s, z_s)$  to the element  $(x_i, 0)$  of the array is:

$$\tau_2(x_s, z_s, x_i) = \frac{1}{c} \sqrt{(x_s - x_i)^2 + z_s^2}. \quad (2)$$

The total time delay from the focused source to the element  $i$  is:

$$\tau_i(x_s, z_s) = \tau_1(x_s, z_s) + \tau_2(x_s, z_s, x_i). \quad (3)$$

If we subtract the total delay time of element  $i$  in (3) from that of element  $j$ , we have:

$$\Delta\tau_{ij} = \frac{1}{c} \left( \sqrt{(x_s - x_i)^2 + z_s^2} - \sqrt{(x_s - x_j)^2 + z_s^2} \right). \quad (4)$$

This time delay  $\Delta\hat{\tau}_{ij}$  can be estimated by correlating the prebeamformed RF signals between element  $i$  and  $j$ . The error between the theoretical value in (4) and the estimated value is:

$$\varepsilon_{ij}(x_s, z_s) = \frac{1}{c} \left[ \sqrt{(x_s - x_i)^2 + z_s^2} - \sqrt{(x_s - x_j)^2 + z_s^2} \right] - \Delta\hat{\tau}_{ij} \quad (5)$$

The only unknown in equation (5) is the point target position  $(x_s, z_s)$ . The estimated point target position  $(\hat{x}_s, \hat{z}_s)$ , can be found by minimizing the sum of squared errors in Eq. (5) over the different pair of elements  $i$  and  $j$  of the linear array,

$$(\hat{x}_s, \hat{z}_s) = \arg \min_{(x_s, z_s)} \sum_{i,j} \varepsilon_{ij}^2(x_s, z_s). \quad (6)$$

The Jacobian of the error in (5) can be explicitly precalculated to speed up the minimization of (6) and provides more robust estimates:

$$\frac{\partial \varepsilon_i}{\partial x_s} = \frac{1}{c} \left[ \frac{x_s - x_i}{\sqrt{(x_s - x_i)^2 + z_s^2}} - \frac{x_s - x_j}{\sqrt{(x_s - x_j)^2 + z_s^2}} \right], \quad (7)$$

$$\frac{\partial \varepsilon_i}{\partial z_s} = \frac{1}{c} \left[ \frac{z_s}{\sqrt{(x_s - x_i)^2 + z_s^2}} - \frac{z_s}{\sqrt{(x_s - x_j)^2 + z_s^2}} \right]. \quad (8)$$

The beam visualization and superposition on the B-mode image are possible with registration of the FUS source with respect to the linear array. After the positions of  $K$  point targets are estimated, we can proceed to estimate the position of the FUS source  $(x_t, z_t)$  by minimizing the following cost function:

$$C = \sum_{k=1}^K \left( \hat{\tau}_1(x_s^k, z_s^k) - \frac{1}{c} \sqrt{(x_s^k - x_t)^2 + (z_s^k - z_t)^2} \right)^2 \quad (9)$$

where  $\hat{\tau}_1(x_s^k, z_s^k)$  is the estimated travel time between the FUS transducer and the point target  $(x_s^k, z_s^k)$ , which can be found by operating the transducer in pulse-echo mode. The same least squares optimization procedure can be applied to find  $(x_t, z_t)$ . By moving the point target in the field of the FUS transducer, different realizations can be obtained providing an estimate of  $(x_t, z_t)$ , i.e., the summation in Eq. (9) is over the different point target locations. This reduces the error in the estimate of the position of the FUS transducer with respect to the array position. The estimated position  $(x_t, z_t)$  is then used in the delay calculations for bistatic beamforming.

2) *Bistatic Beamforming*: The traditional delay and sum approach to beamforming was modified for the bistatic setup. A fixed subaperture of size  $2N+1$  was chosen with a center element  $x_c$  and the channel data used for beamforming were acquired from elements  $x_{c-N}$  to  $x_{c+N}$  (see Fig. 4). Using these channel data, the beamformed values were calculated along the line going through  $x_c$  and perpendicular to the x-axis. The resulting image was a vertical stack of beamformed lines for all the elements in the array.

The time delay from the FUS source ( $x_t, z_t$ ) to a scatterer located at ( $x_s, z_s$ ) and then to the array element ( $x_i, 0$ ) is:

$$\tau_{ic} = \frac{\sqrt{(x_s - x_t)^2 + (z_s - z_t)^2}}{c} + \frac{\sqrt{(x_s - x_i)^2 + z_s^2}}{c}, \quad (10)$$

where  $c$  is the sound speed assumed to be 1540 m/s.

The beamformed value at each location ( $x_s, z_s$ ) of the line going through  $x_c$  was found by applying the delay in Eq. (10) for each element in the subaperture and summing them:

$$I_c(x_s, z_s) = \frac{1}{2N+1} \sum_{i=-N}^N s_i[n - \tau_{ic}], \quad (11)$$

where  $s_i[n]$  is the channel data from element  $i$ . If the delay  $\tau_{ic}$  is not an integer, linear interpolation of the two values of  $s_i[n - \lfloor \tau_{ic} \rfloor]$  and  $s_i[n - \lfloor \tau_{ic} \rfloor + 1]$  was used, where  $\lfloor \tau_{ic} \rfloor$  is the closest integer to  $\tau_{ic}$ . A Hanning window was applied to all the RF channel data in each subaperture to reduce the effect of sidelobes. Different subaperture sizes were explored: 17, 33, 49 and 65. A subaperture size of 65 was found to give the best result and was subsequently used to produce all images shown. Near the edge of array, where part of the subaperture is outside of the physical array (element index  $c - N$  is less than zero or  $c + N$  is larger than 128), an aperture of less than 65 is used, i.e. from element  $\max(c - N, 0)$  to element  $\min(c + N, 128)$ . For example, if the center element  $x_c$  is 10, elements from 1 to 43 are used for beamforming.

### C. Performance Metrics

To quantify the accuracy of the beam visualization constructed from scattering arising in the sample, the reconstructions from the homogeneous phantom were compared to beam reconstructions from a single wire target that was used to map the field of the FUS source. Specifically, a tungsten wire target (50  $\mu\text{m}$  diameter) was placed in the field of the array and FUS transducer, perpendicular to the image plane of the array and the beam axis of the FUS source. The wire was static while the holder was moved using the positioning system, effectively mapping out the beam of the FUS source [32]. The positioning system was moved over a rectangular region with an axial length of 20 mm (along the beam axis) and lateral length of 2 mm (cross beam axis). The focus of the FUS transducer was at the center of this rectangle. The axial and lateral scanning steps were 0.1 mm and 0.5 mm respectively (the axial and lateral axes are x-axis and z axis in Fig. 4). For each scanning step, the SonixOne simultaneously triggered the Panametrics 5800 to pulse excite the FUS transducer and initiated the SonixDAQ to passively

listen via the linear array. The bistatic beamforming method was used to map the intensity at each point in the depth of field of the FUS transducer. The resulting reconstructed field from the FUS transducer would be a convolution of the beam of the FUS transducer, the scattering from the wire and the beamformed field characteristics of the array at each point. The  $-6$ -dB bistatic beamwidth and depth of field of the resulting reconstructions were estimated from the wire image and the reconstruction from the homogeneous phantom and compared.

With the wire target approach, only a single scatterer would be in the field at each point and the beam reconstruction would not have speckle. This would provide a smooth reconstruction of the beam profile. To reconstruct the field from the FUS transducer using a translated wire, a pulse excitation is needed for each point in the field as the wire moves throughout the field. On the other hand, when reconstructing the FUS transducer field from a sample containing many randomly spaced scatterers, e.g., the homogeneous phantom, only a single pulse excitation is needed. However, the resulting reconstruction is the beam intensity field superimposed with a speckle background. To better compare the beamwidth estimates from the wire target and from the homogeneous phantom, speckle reduction techniques were employed on the reconstruction from the homogeneous phantom. Specifically, multiple reconstructions from independent planes within the homogeneous sample were created and compounded together to reduce speckle variance.

The beamwidth and depth-of-field estimates from the wire targets and the homogeneous phantom were also compared to theoretical values. For the FUS transducer with frequency of 6 MHz, the wavelength is approximately 250  $\mu\text{m}$ . Theoretically, the  $-3$ -dB transmit or  $-6$ -dB transmit-receive beamwidth and depth of field are [32]:

$$R_L = 1.028\lambda f_{\#} = 1.028 * 0.25 * 2 = 0.5 \text{ mm}. \quad (12)$$

$$Z_F(3\text{dB}) = 7.08\lambda * (f_{\#}^2) = 7.08 * 0.25 * 4 = 7.08 \text{ mm}. \quad (13)$$

## III. RESULTS

Figure 5(a) shows the transmit beam pattern estimated from the hydrophone measurements of the FUS source. The needle hydrophone was swept through the focal zone of the FUS source in pulsed excitation mode. The pulse intensity integral of the RF signal received by the hydrophone was calculated at each position and was normalized to generate the spatial map. The axial and lateral scanning steps were 200  $\mu\text{m}$ . The estimated  $-3$ -dB transmit ( $-6$ -dB transmit-receive) beamwidth and depth of field were 0.51 mm and 7.1 mm, respectively, which agrees with the theoretical prediction in Eqs. (12) and (13).

Figure 5(b) shows the passive beam map generated by moving the tungsten wire through the focal region of the FUS transducer. The FUS transducer is on the left of the image. The axial and lateral axes are defined with respect to the linear array oriented at the top of the figure. For each wire position, the bistatic delay and sum approach was applied to prebeamformed RF data to generate a field map. All of the field maps were envelope detected and averaged

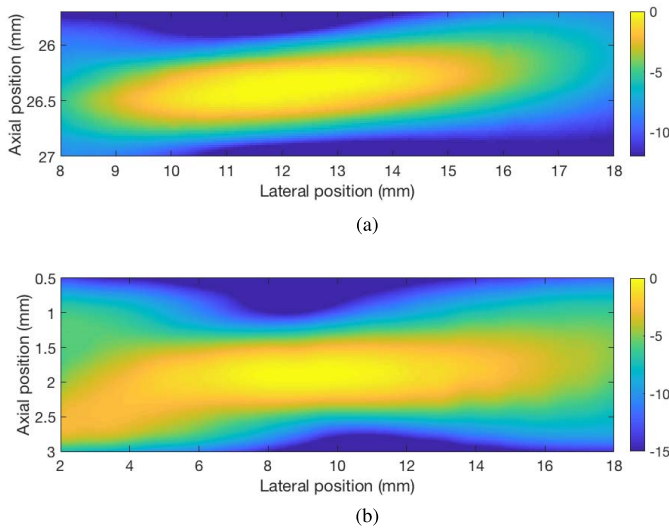


**Fig. 5.** (a) Hydrophone determined beam of the 6-MHz  $f/2$  FUS transducer alone. The measured transmit  $-3$ -dB beamwidth and depth of field were 0.51 mm and 7.1 mm, respectively. (b) Passive map of the focused field constructed using the wire technique. The estimated beamwidth and depth of field were 1.2 mm and 16.8 mm, respectively. Note that the beam construction using the wire is affected by both the FUS source and the listening array characteristics.

to generate Fig. 5(b). The  $-6$ -dB beamwidth and depth of field in the bistatic case were estimated to be 1.2 and 16.8 mm, respectively. The larger beamwidth in the bistatic setup compared to the hydrophone reconstruction of the beam was due to addition of the point spread function (PSF) of the linear array. Fig. 7 plotted the beamformed image of one of the wire locations used in Fig. 5(b), specifically at the axial and lateral location of 29.4 mm and 13.6 mm, respectively. It is assumed that the scatter from the wire corresponds closely to the actual PSF of the combined FUS source and passive array using the described beamforming techniques. The  $-6$ -dB axial beamwidth of the bistatic PSF in Fig. 7 was measured to be 0.89 mm. The passive wire map in Figure 5(b) is the convolution of the beam of the FUS source and the bistatic PSF. Assuming the two beams can be approximated by Gaussian functions, the beamwidth of the resulting convolution, i.e. the bistatic wire mapping, is  $\sqrt{0.89^2 + 0.705^2} = 1.14$  mm, where the  $-6$ -dB beamwidth of the FUS source is 0.705 mm and the  $-6$ -dB axial beamwidth of the array is 0.89 mm. The theoretical prediction of 1.14 mm is close to the measured value of 1.2 mm.

Figure 6(a) shows the image of the beam reconstructed from the homogeneous phantom from a single shot of the FUS source. The image shows the intensity variance throughout the beam, which is caused by speckle, and complicates estimation of the beam characteristics. However, the single shot reconstruction still preserves the shape and dimension of the beam when compared to Fig. 6(b) of the compounded image. Fig. 6(b) shows the reconstructed image of the beam of the single-element FUS transducer from the scattered fields produced in the homogeneous tissue-mimicking phantom when compounding from independent image planes. As before, the single-element FUS transducer is pulse excited once and

**TABLE I**  
ESTIMATED  $-6$  dB BEAMWIDTH AND DEPTH OF FIELD FOR THE TRANSMIT ONLY, BISTATIC SET-UP AND HOMOGENEOUS PHANTOM

	Hydrophone determined	Wire target	Homogeneous phantom
Beamwidth	0.51 mm	1.2 mm	1.5 mm
Depth of field	7.1 mm	16.8 mm	11.8 mm

the fields scattered throughout the phantom are received by the listening array. The visualization of the beam is reconstructed by focusing the ultrasound recorded on the listening array at each point in the field. The images in Fig. 6(b) and 6(c) were the result of compounding five different snapshots of the phantom from five independent positions by physically moving the phantom. The  $-6$ -dB bistatic beamwidth and depth of field were estimated to be 1.5 mm and 11.8 mm, respectively, which are comparable to the  $-6$ -dB focal zone dimension of the passive wire map (1.2 mm by 16.8 mm). The depth of field was underestimated due to the speckle. Figure 6(d) shows a zoomed out version of Fig. 5(b) such that the dimensions of the field of view are matched to the beam reconstructions from the rest of Fig. 6. Comparing Figs. 6(b) with 6(d) shows that the beam reconstructions from the phantom and the wire were of similar size over the dimensions for which the wire target was moved throughout the field. However, the flaring out of the beam at the edges of the depth of field that was visualized in the phantom reconstruction was not imaged by the wire reconstruction because the wire was only moved through a small rectangle intended to capture the depth of field of the FUS source. Table I lists the estimated beam characteristics from the wire target for the transmit only case using the hydrophone, the bistatic configuration with the wire target and the bistatic configuration with the homogeneous phantom reconstructions. Fig. 6(c) shows the bistatic reconstructed beam of the single-element FUS transducer overlaid onto the B-mode image. The beam can be visualized *in situ* within the phantom and is denoted by the color overlay whereas the B-mode image is in grayscale. The smallest 10 dB values in the color beam map (dark blue color and smaller than  $-30$  dB) were not displayed to make the B-mode image more visible.

Figure 8(a) shows the bistatic reconstructed beam when insonifying a two-layered phantom. The focused source was insonifying from the left of the figure and the linear array was receiving from the top of the figure. The glass bead density in the right layer was 10 times higher than in the left layer, which is predicted to result in an increase in image intensity of 10 dB in the B-mode image. The beam region in the right layer from the lateral distance of 15 to 20 mm (shown red in Fig. 8) is 10 dB higher than the beam immediately to the left of the layer, indicating that the beamforming technique was affected by the intensity changes in the sample.

The change in the scattering characteristics resulted in the reconstructed beam suppressing the beam profile in the low-density medium as compared to the higher glass bead density layer. As a result, the beam appears to widen out as it enters the brighter region. To partially account for the layering effect, the registered B-mode image was used to correct intensity discontinuities in the FUS beam reconstruction due to the

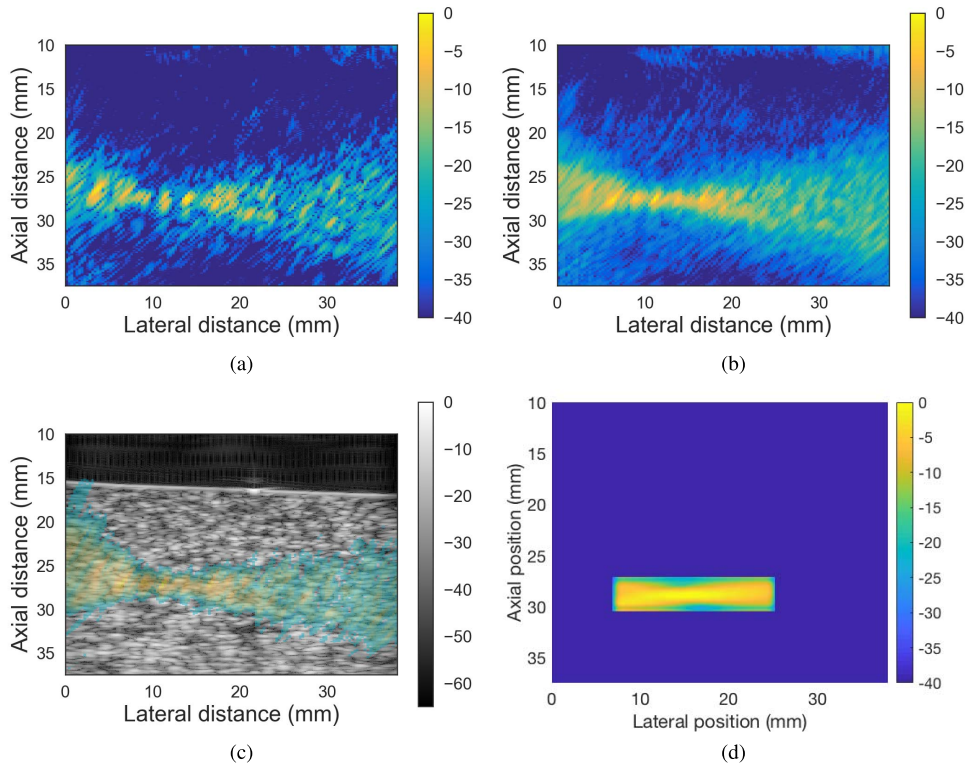


Fig. 6. (a) Single shot of the passive beam image of the homogeneous phantom. (b) Compounded image of the passive beam images in the homogeneous phantom. (c) Overlaid compounded beam on the B-mode image of the homogeneous phantom. (d) Bistatic beam estimated using the wire target. The  $-6$ -dB bistatic beamwidth and depth of field were estimated to be 1.5 mm and 11.8 mm, respectively.

inhomogeneity in the scattering medium. To introduce the correction to the FUS beam reconstruction, 26 overlapping rectangular sections of size 5 mm axially by 38 mm laterally were extracted from the registered B-mode image. These sections were centered around the depth of the FUS source, from 20 mm to 32 mm with a step size of 0.5 mm. The intensity values in dB of each region were averaged along the axial dimension. The mean was subtracted from the averaged line along the 38 mm lateral length and the zero crossing of this line was calculated to detect the discontinuity between the two layers (see Fig. 9). The mean dB value from the higher intensity layer (shown in green) was subtracted from the lower intensity layer (shown in blue) to get the dB difference between the layers. The dB differences between two layers were estimated and averaged over all sections to give a mean value of 9.6 dB, which was converted to linear scale  $10^{\frac{9.6}{20}} = 3.02$  and the passive FUS beam reconstruction corresponding to the lower glass bead density was multiplied by this factor. The rescaled enveloped-detected passive beam image was normalized to 0 dB and the corrected FUS beam reconstruction is shown in Fig. 8(c).

The rescaling of the FUS beam provides the visualization of an interesting behavior where the beam at the intersection appears to transmit through the layer but also reflects off of the layer at an angle heading downward and back towards the FUS source. The bistatic beamforming algorithm uses the assumption that the FUS source propagates its beam in a direction that is approximately parallel to the face of the listening array. Hence, signals generated closer to the

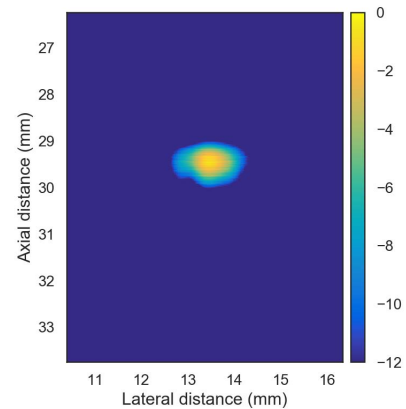


Fig. 7. Point spread function of bistatic beamforming at the wire location  $x = 13.6$  mm,  $z = 29.4$  mm.

FUS source, i.e., the left side of the array, will arrive earlier at the array than signals generated further from the FUS source, even though these signals are coming from close to the same depth with respect to the surface of the array. Therefore, ultrasound that is reflected from an interface and propagates back towards the FUS source, results in signals generated from scatterer locations that are progressively closer to the FUS source at approximately the same depth with regard to the array but arriving with delays in time at the array that make it look as though the signals are coming from deeper. When beamforming these reflected signals, two things occur: 1) The signals are assumed to come from greater depths than

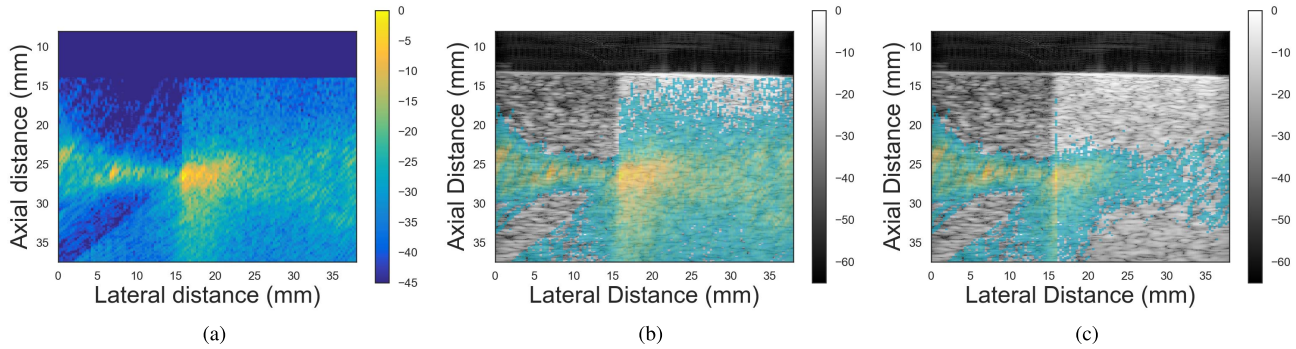


Fig. 8. Two-layered phantom of different glass bead density. (a). Reconstructed passive beam image. (b). Overlay of the beam onto the B-mode image. (c) FUS beam reconstructed using an intensity mask created from the B-mode image.

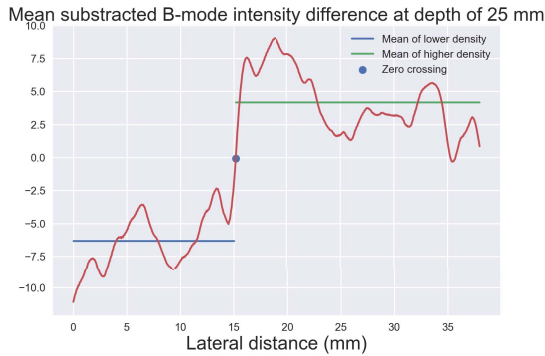


Fig. 9. Depiction of the zero-mean intensity line across the two layer phantom. The difference between two levels was used to correct for intensity variations in the reconstructed FUS beam.

they really are, which causes the time delays for focusing from the listening array to incorrectly focus resulting in a broadening of the beam visualization of the reflected wave. 2) As the ultrasound propagates back towards the FUS source, the signals are progressively delayed in reaching the array and are assumed to come from greater depths when beamforming, which causes the visualization of the reflected beam to look as though it is coming from progressively greater depths as it propagates towards the FUS source, i.e., the reflected beam is rotated by approximately  $45^\circ$  away from the array surface. This reflection artifact of the bistatic configuration would not occur if the FUS source and the linear array were in a monostatic configuration, i.e., if the listening array were placed in line with the FUS source.

Figure 10(a) shows the reconstructed beam of the single-element FUS transducer when insonifying a chicken breast. The passive beam image was formed by compounding four different realizations of the single snapshot of the bistatic beam image by physically translating the FUS source and linear array setup by 0.5 mm for each realization. The FUS source and linear array were both translated parallel to the chicken breast. The same scatterers in the chicken breast that produce speckle were used to provide the beam reconstruction. Figure 10(b) shows the beam insonifying the chicken breast overlaid on the B-mode image (grayscale).

#### IV. DISCUSSION

The purpose of the study was to demonstrate a novel mapping technique that allowed the reconstruction and

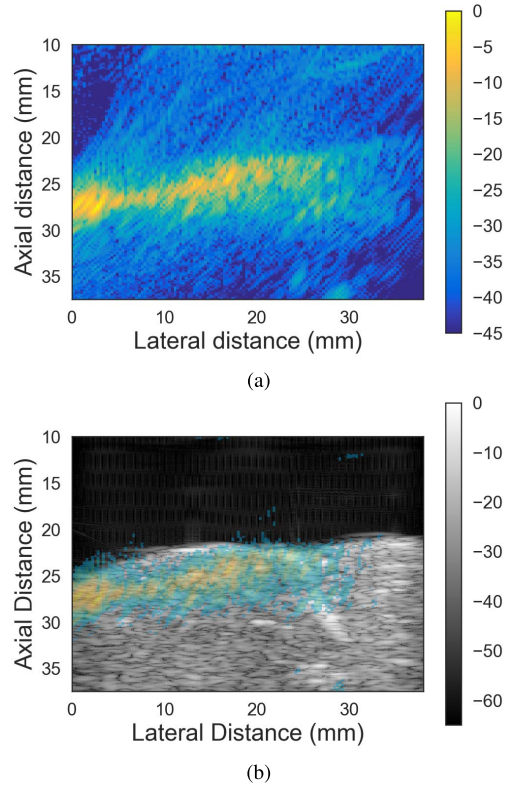


Fig. 10. (a) Reconstructed passive beam image in the chicken breast. (b) Overlay of the beam onto the B-mode image of the chicken breast.

visualization of the beam from a FUS source *in situ*. Visualizing the beam from the FUS source *in situ* enables better monitoring and planning of FUS-based therapy because the therapy beam can be imaged continuously in the context of its location in a tissue region. By continuously imaging the beam of the FUS source, the location of the beam can be adjusted when tissue motion occurs causing the beam to translate from the targeted therapy region. We demonstrated the ability to visualize the beam from a FUS source in three separate samples: a homogeneous tissue-mimicking phantom, a two-layered phantom and in a chicken breast sample.

To quantify the accuracy of our technique for reconstructing the field from a FUS source *in situ*, the field of the FUS source was also mapped out by moving a single wire target throughout the field of the FUS source and mapping the

intensity at each point in the field both with transmit-only using a hydrophone and with the bistatic configuration. Comparisons of the FUS field from the homogeneous phantom and the wire (Figs. 6(b) and 6(d), respectively) suggest that the *in situ* visualization could provide a good representation of the beam location and extent. The field reconstructed from the wire target in the bistatic configuration had beam properties that corresponded well to properties that were acquired from the homogeneous phantom. Specifically, the measured  $-6$ -dB bistatic beamwidth and depth of field estimated from the wire mapping were 1.2 mm and 16.8 mm, respectively, which compared to 1.5 mm and 11.8 mm from the homogeneous phantom. The beam in Figure 5(b) is the convolution of the beam of the FUS source and the bistatic PSF, which is plotted in Fig 7. Under the Gaussian beam approximation, the prediction of 1.14 mm is close to the measured value of 1.2 mm.

The approach to passive mapping of scatterers in the homogeneous phantom was equivalent to the wire mapping except the whole field throughout the beam could be acquired using a single excitation when using a medium with many randomly located scatterers, e.g., the homogeneous phantom. Unlike the beam mapped from the wire, which is a single point scatterer translated throughout the field, the beam representation from the homogeneous phantom was not continuous but rather appeared as the field intensity of the beam but with a speckle pattern. A single shot of the homogeneous phantom preserves the general geometry of the beam with the narrow neck in the middle. However, spatial compounding of beam images from several independent planes in the homogeneous phantom smoothed out the representation of the field, i.e., reduced the speckle, as shown in Figure 6(a) and 6(b). Therefore, the more images used in the spatial compounding, the clearer the pattern of the beam that emerged due to smoothing of the speckle. In practice, such spatial compounding would not occur during therapy monitoring because presumably the beam would remain on the same location during therapy. Therefore, other speckle reduction techniques, such as frequency compounding or application of speckle filters, could be explored to reduce the speckle artifact in the beam visualization.

The reconstructed field could be superimposed on B-mode images to give anatomical context of the location of the FUS transducer beam in a tissue, as demonstrated in each of the visualizations. The visualization in the two-layered phantom indicated that the registration technique correctly aligned the FUS beam reconstruction with the B-mode image. However, while we could align the FUS source in the imaging plane of the listening array, from experiment to experiment the FUS source could have some tilt along the axial direction of the imaging plane. For example, the beam visualization is observed to tilt upward for the homogeneous phantom, had almost no tilt for the two layer phantom and had a downward tilt for the chicken breast. The technique was able to capture these slight tilts in the alignment. In the bistatic configuration, because there are two unknowns ( $x_t, z_t$ ) in equation (9), we need at least two independent wire target estimations ( $x_s, z_s$ ) to solve the registration problem of placing the passive beam image onto the B-mode image. In our experiments,

we used five randomly-positioned wire targets from the wire-target mapping experiment to register the FUS source position.

In terms of intensity variations in the beam profile, we confirmed that higher intensity variations in the corresponding B-mode image, due to structures in the tissues like bright specular scatterers or tissue interfaces, could be used to correct for image intensity variations in the FUS field pattern visualization. The visualizations from the two-layered phantom demonstrated the ability to visualize the beam in regions having different scattering properties. The beam intensity contrast followed closely the B-mode image contrast of the medium. The intensity of the beam in the medium with higher glass bead density (by a factor of 10 times) was 10 dB higher. The beam intensity increased where the layer occurred as portrayed in the superimposed image of Fig. 8. Interestingly, by applying the correction to the FUS beam reconstruction based on the registered B-mode image, reflection behaviors of the ultrasound field at the interface were revealed. Hence, the technique has the potential to visualize the beam location and how it may reflect and refract in media with interfaces. This would be helpful in ensuring that therapy beams are targeting specific tissue regions where different tissue interfaces may be present.

The beamforming algorithm assumed a fixed speed of sound in the medium, which is a function of the temperature during ablation. Effects of phase aberration due to incorrect sound speed assumptions were not explored in this work. A speed of sound estimation algorithm such as [22] could be incorporated to update the beam image.

Compared to the monostatic approach, the bistatic approach removes the need of manufacturing a FUS source with a cutout for a linear array. However, the bistatic approach requires an alignment step to ensure the beam visualization can be properly superimposed on the B-mode image. Furthermore, a bistatic approach may not be feasible for many therapy setup conditions where only the backscatter could be measured. The bistatic registration formulation is general enough in setups with angles other than  $90^\circ$  between the FUS source and the linear array.

The passive FUS beam visualization method has similarities to passive cavitation mapping, yet, is also distinct. First, cavitation mapping provides a visualization of the passive array beam convolved with the cavitation signal at the spatial location of the cavitation event. While these events likely occur within the spatial location of the FUS beam, the mapping is not of the actual FUS beam. Second, in our approach the passive recording is synchronized with the excitation from the FUS source. Hence, the absolute time of flight allows determination of the depth of the acoustic emission. Third, the delay and sum beamforming was not integrated using the time exposure acoustics algorithm for passive cavitation mapping to improve the resolution of broadband noise [28]. The beamforming equations we utilized are different (i.e., no integration step). Fourth, the registration of the FUS source for estimating the exact geometry of the experiment was explicit, allowing the correct positioning of the beam in the B-mode image. Finally, the registered B-mode image was used to correct for intensity variations in the FUS beam reconstruction.

## V. CONCLUSION

In this study, we demonstrated the ability to visualize the beam of a FUS source *in situ* in a bistatic configuration where a linear array imaging probe was aligned at a 90° angle with FUS transducer, i.e., a bistatic configuration. Delay and sum beamforming was utilized by the listening array to focus the receive signal at each point in the field from which ultrasound was scattered. Using the same array a registered B-mode image of the sample was also constructed. The FUS-beam visualization was then superimposed on top of the registered B-mode image to visualize the FUS beam *in situ*. Variations in the reconstructed FUS-beam intensity could be corrected by utilizing the intensity variations in the registered B-mode image. FUS-beam visualization *in situ* can provide anatomical context for FUS therapy monitoring and planning.

## REFERENCES

- [1] I. Mindjuk, C. G. Trumm, P. Herzog, R. Stahl, and M. Matzko, "MRI predictors of clinical success in MR-guided focused ultrasound (MRgFUS) treatments of uterine fibroids: Results from a single centre," *Eur. Radiol.*, vol. 25, no. 5, pp. 1317–1328, 2015.
- [2] M. D. Hurwitz *et al.*, "Magnetic resonance-guided focused ultrasound for patients with painful bone metastases: Phase III trial results," *J. Nat. Cancer Inst.*, vol. 106, no. 5, pp. 1–9, 2014.
- [3] S. Crouzet *et al.*, "Whole-gland ablation of localized prostate cancer with high-intensity focused ultrasound: Oncologic outcomes and morbidity in 1002 patients," *Eur. Urol.*, vol. 65, no. 5, pp. 907–914, 2014.
- [4] W. J. Elias *et al.*, "A randomized trial of focused ultrasound thalamotomy for essential tremor," *New England J. Med.*, vol. 375, no. 8, pp. 730–739, 2016.
- [5] N. McDannold, G. T. Clement, P. Black, F. Jolesz, and K. Hynynen, "Transcranial magnetic resonance imaging-guided focused ultrasound surgery of brain tumors: Initial findings in 3 patients," *Neurosurgery*, vol. 66, no. 2, pp. 323–332, 2010.
- [6] F. Wu *et al.*, "A randomised clinical trial of high-intensity focused ultrasound ablation for the treatment of patients with localised breast cancer," *British J. Cancer*, vol. 89, no. 12, pp. 2227–2233, 2003.
- [7] A. Burgess, Y. Huang, A. C. Waspe, M. Ganguly, D. E. Goertz, and K. Hynynen, "High-intensity focused ultrasound (HIFU) for dissolution of clots in a rabbit model of embolic stroke," *PLoS ONE*, vol. 7, no. 8, p. e42311, 2012.
- [8] A. Podkowa, R. J. Miller, R. W. Motl, and M. L. Oelze, "Focused ultrasound therapy of cervical lymph nodes in rats for alleviating multiple sclerosis symptoms," *J. Acoust. Soc. Amer.*, vol. 140, no. 4, p. 3373, 2016.
- [9] C. Maleke and E. E. Konofagou, "Harmonic motion imaging for focused ultrasound (HMIFU): A fully integrated technique for sonication and monitoring of thermal ablation in tissues," *Phys. Med. Biol.*, vol. 53, no. 6, p. 1773, 2008.
- [10] W. Legon *et al.*, "Transcranial focused ultrasound modulates the activity of primary somatosensory cortex in humans," *Nature Neurosci.*, vol. 17, no. 2, pp. 322–329, 2014.
- [11] J. C. Bamber and C. R. Hill, "Ultrasonic attenuation and propagation speed in mammalian tissues as a function of temperature," *Ultrasound Med. Biol.*, vol. 5, no. 2, pp. 149–157, 1979.
- [12] C. W. Song, A. Lokshina, J. G. Rhee, M. Patten, and S. H. Levitt, "Implication of blood flow in hyperthermic treatment of tumors," *IEEE Trans. Biomed. Eng.*, vol. BME-31, no. 1, pp. 9–16, Jan. 1984.
- [13] C. Damianou and K. Hynynen, "The effect of various physical parameters on the size and shape of necrosed tissue volume during ultrasound surgery," *J. Acoust. Soc. Amer.*, vol. 95, no. 3, pp. 1641–1649, 1994.
- [14] N. I. Vykhodtseva, K. Hynynen, and C. Damianou, "Pulse duration and peak intensity during focused ultrasound surgery: Theoretical and experimental effects in rabbit brain *in vivo*," *Ultrasound Med. Biol.*, vol. 20, no. 9, pp. 987–1000, 1994.
- [15] B. Quesson *et al.*, "Real-time volumetric MRI thermometry of focused ultrasound ablation *in vivo*: A feasibility study in pig liver and kidney," *NMR Biomed.*, vol. 24, no. 2, pp. 145–153, 2011.
- [16] M. Marx, P. Ghanouni, and K. B. Pauly, "Specialized volumetric thermometry for improved guidance of MRgFUS in brain," *Magn. Reson. Med.*, vol. 78, no. 2, pp. 508–517, 2016.
- [17] G. J. Czarnota *et al.*, "Tumor radiation response enhancement by acoustical stimulation of the vasculature," *Proc. Nat. Acad. Sci. USA*, vol. 109, no. 30, pp. E2033–E2041, 2012.
- [18] K. Hynynen, N. McDannold, N. A. Sheikov, F. A. Jolesz, and N. Vykhodtseva, "Local and reversible blood-brain barrier disruption by noninvasive focused ultrasound at frequencies suitable for trans-skull sonications," *NeuroImage*, vol. 24, no. 1, pp. 12–20, 2005.
- [19] M. Kinoshita, N. McDannold, F. A. Jolesz, and K. Hynynen, "Non-invasive localized delivery of herceptin to the mouse brain by MRI-guided focused ultrasound-induced blood-brain barrier disruption," *Proc. Nat. Acad. Sci. USA*, vol. 103, no. 31, pp. 11719–11723, 2006.
- [20] J. J. Choi, M. Pernot, S. A. Small, and E. E. Konofagou, "Noninvasive, transcranial and localized opening of the blood-brain barrier using focused ultrasound in mice," *Ultrasound Med. Biol.*, vol. 33, no. 1, pp. 95–104, Jan. 2007.
- [21] K. Hynynen, N. McDannold, N. Vykhodtseva, and F. A. Jolesz, "Non-invasive MR imaging-guided focal opening of the blood-brain barrier in rabbits," *Radiology*, vol. 220, no. 3, pp. 640–646, Sep. 2001.
- [22] C. Simon, P. VanBaren, and E. S. Ebbini, "Two-dimensional temperature estimation using diagnostic ultrasound," *IEEE Trans. Ultrason., Ferroelectr., Freq. Control*, vol. 45, no. 4, pp. 1088–1099, Jul. 1998.
- [23] F. L. Lizzi *et al.*, "Radiation-force technique to monitor lesions during ultrasonic therapy," *Ultrasound Med. Biol.*, vol. 29, no. 11, pp. 1593–1605, 2003.
- [24] M. Fujiwara, K. Nakatsuma, M. Takahashi, and H. Shinoda, "Remote measurement of surface compliance distribution using ultrasound radiation pressure," in *Proc. IEEE World Haptics Conf. (WHC)*, Jun. 2011, pp. 43–47.
- [25] A. J. Casper, D. Liu, J. R. Ballard, and E. S. Ebbini, "Real-time implementation of a dual-mode ultrasound array system: *In vivo* results," *IEEE Trans. Biomed. Eng.*, vol. 60, no. 10, pp. 2751–2759, Oct. 2013.
- [26] V. A. Salgaonkar, S. Datta, C. K. Holland, and D. T. Mast, "Passive cavitation imaging with ultrasound arrays," *J. Acoust. Soc. Amer.*, vol. 126, no. 6, pp. 3071–3083, 2009.
- [27] M. Gyöngy and C. C. Coussios, "Passive spatial mapping of inertial cavitation during HIFU exposure," *IEEE Trans. Biomed. Eng.*, vol. 57, no. 1, pp. 48–56, Jan. 2010.
- [28] C. R. Jensen, R. W. Ritchie, M. Gyöngy, J. R. T. Collin, T. Leslie, and C. C. Coussios, "Spatiotemporal monitoring of high-intensity focused ultrasound therapy with passive acoustic mapping," *Radiology*, vol. 262, no. 1, pp. 252–261, 2012.
- [29] K. J. Haworth *et al.*, "Passive imaging with pulsed ultrasound insonations," *J. Acoust. Soc. Amer.*, vol. 132, no. 1, p. 544, 2012.
- [30] K. J. Haworth, K. B. Bader, K. T. Rich, C. K. Holland, and T. D. Mast, "Quantitative frequency-domain passive cavitation imaging," *IEEE Trans. Ultrason., Ferroelectr., Freq. Control*, vol. 64, no. 1, pp. 177–191, Jan. 2017.
- [31] M. T. Burgess, I. Apostolakis, and E. E. Konofagou, "Power cavitation-guided blood-brain barrier opening with focused ultrasound and microbubbles," *Phys. Med. Biol.*, vol. 63, no. 6, p. 065009, 2018.
- [32] K. Raum and W. D. O'Brien, "Pulse-echo field distribution measurement technique for high-frequency ultrasound sources," *IEEE Trans. Ultrason., Ferroelectr., Freq. Control*, vol. 44, no. 4, pp. 810–815, Jul. 1997.